Electronic Research Archive

ERA, 33(11): 6700–6719.
DOI: 10.3934/era.2025296
Received: 06 September 2025
Revised: 01 November 2025
Accepted: 06 November 2025
Published: 13 November 2025

http://www.aimspress.com/journal/era

Research article

Sliding mode control of electro-hydraulic servo based on neural network adaptive observer

Chungeng Sun*, Shengyou Chen and Zhenlong Deng

Faculty of Mechanical and Electrical Engineering, Kunming University of Science and Technology, Kunming 650500, China

* **Correspondence:** Email: cgsun@kust.edu.cn.

Abstract: This paper addresses the common challenges of multi-source nonlinear disturbances and parameter uncertainties in traditional electro-hydraulic servo systems by proposing an enhanced sliding mode control method based on a neural network adaptive observer. First, a nonlinear mathematical model of the electro-hydraulic system was established based on the structure and working principle of the valve-controlled hydraulic cylinder. Second, by leveraging the strong nonlinear approximation capability of radial basis function (RBF) neural networks, the nonlinear terms in the system were approximated online and compensated in real time. Next, an adaptive state observer utilizing RBF neural networks was developed to precisely estimate the difficult-to-measure states within the hydraulic system. The state estimates from the observer were integrated with sliding mode control to design the system control law. Additionally, a low-pass filter was introduced to smooth the control law, improving the smoothness of the controller's output and the overall system stability. Finally, the bounded stability of the closed-loop system was proven by constructing a Lyapunov function. Simulation results demonstrate that under various reference signal inputs and parameter abrupt change scenarios, the designed controller exhibits faster convergence and superior robustness compared to traditional nonlinear controllers. Its average tracking error is reduced by 27.51%–90.2% relative to the intelligent PID controller and by 14.55%–68.82% relative to the adaptive sliding mode controller (ASMC). It exhibits notable improvements in control precision, dynamic response velocity, and disturbance rejection performance, thereby offering an efficient approach to addressing nonlinear control challenges in electro-hydraulic servo systems.

Keywords: electro-hydraulic servo; neural network; observer; sliding mode control

1. Introduction

The electro-hydraulic servo system combines a hydraulic actuator with an electronic controller, enabling it not only to deliver large power output but also to achieve high-precision control, with applications spanning aerospace, military, metallurgy, and ships [1–5]. Electro-hydraulic servo systems exhibit several nonlinear characteristics, primarily including saturation, gap, friction, and hysteresis loop [6]. These characteristics reduce the responsiveness and control accuracy of the system and lead to uncertainty in the output response [7]. The presence of various nonlinear factors complicates the study and analysis of electro-hydraulic servo systems. Consequently, conventional control methods often fail to achieve the desired control performance, making the compensation for these nonlinearities and the development of advanced control strategies key to improving system performance [8–11].

Extensive explorations and researches to further improve the control performance of nonlinear systems have been conducted. Examples include sliding mode control [12–14], fuzzy control [15–17], backstepping control [18–20], and adaptive robust control [21–23]. In response to the challenges of nonlinearity and parameter uncertainty in physical systems, control strategies have evolved from traditional to intelligent and from single methods to composite ones, with gradual applications across multiple technical fields [24–29]. H. Feng et al. [30] designed a terminal sliding mode compensation strategy by fusing adaptive sliding mode control with an RBF neural network, which effectively suppressed the system uncertainty and load perturbation, and significantly improved the trajectory tracking accuracy and robustness of the electro-hydraulic servo system. Q. Guo et al. [31] introduced a fixed-time sliding mode disturbance observer to estimate the centralized uncertainty and implemented a parameter adaptive law to compensate for the dead zone of the hydraulic servo valve in real time. This approach guarantees that the joint trajectory error of the hydraulic manipulator converges within a preset, predetermined fixed time, with the convergence time being independent of the initial conditions. V. Kumar et al. [32] designed a new fuzzy PID controller by discretizing the traditional PID controller through bilinear transformation and integrating it with fuzzy logic, which significantly improves the performance of the nonlinear systems. M. F. Ghani et al. [33] incorporated a fractional-order integral sliding mode surface into the conventional sliding mode control method, designed a fractional-order integral sliding mode controller, and optimized the parameters of the controller by using the particle swarm optimization algorithm, which achieves high-precision tracking and control of multiple target trajectories. A. A. Khater et al. [34] proposed an adaptive fuzzy PI controller based on a deep Q-learning network (DQLN). This approach employs the Lyapunov stability theorem to update Q-network weights online and utilizes DQLN to dynamically adjust fuzzy input and output scaling factors. This enables the electro-hydraulic servo system to rapidly track setpoint speeds under conditions such as load transients, dynamic disturbances, and actuator noise, significantly enhancing control performance. Results demonstrate superior control accuracy and robustness compared to conventional algorithms.

Control methods like sliding mode, fuzzy, and adaptive control have led to some advancements in electro-hydraulic servo systems, which still generally struggle to effectively manage the combined challenges of multiple nonlinearities and significant parameter uncertainties. As a result, these existing approaches often make it difficult to achieve a good balance between transient response, steady-state performance, and disturbance rejection. In order to better solve parameter uncertainty and nonlinear perturbation problems prevailing in hydraulic systems, this paper proposes an improved sliding mode control strategy based on a radial basis function neural network adaptive observer. Using a neural

network state adaptive observer, the system's states are estimated, and a low-pass filtering method is applied to reduce high-frequency noise in the control law while achieving improved tracking performance. Additionally, the controller's asymptotic stability is demonstrated through the Lyapunov function.

2. System model

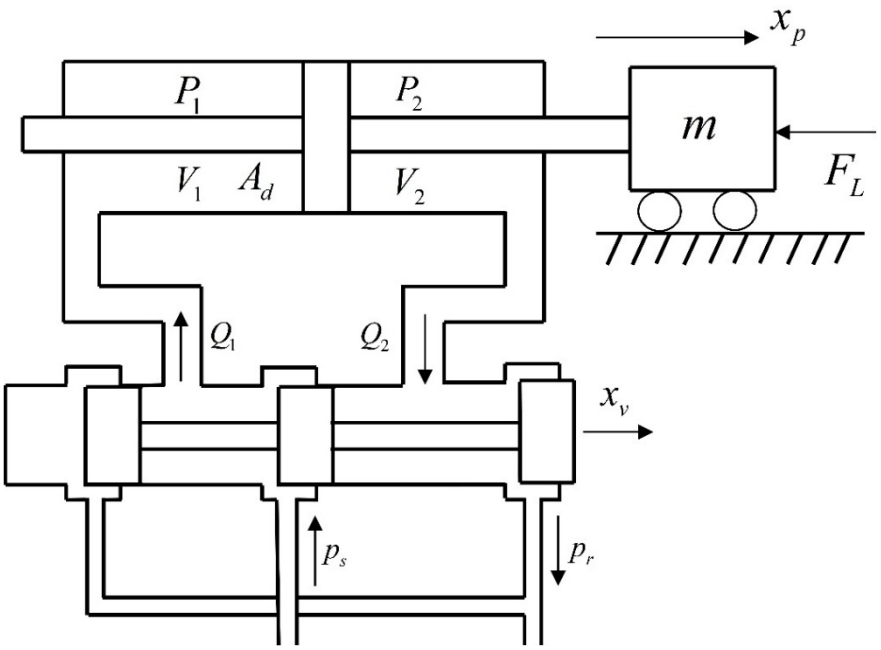

Figure 1. Electro-hydraulic position servo system.

The electro-hydraulic position servo system is shown in Figure 1. According to Newton's second law, the force balance equation of the hydraulic cylinder can be established as:

$$m\ddot{x}_p = p_L A_d - B\dot{x}_p - F_L \tag{1}$$

where m is the equivalent total mass of the piston and the external load referred to the piston; x_p is the piston displacement of the hydraulic cylinder; p_1 and p_2 are the pressures in the left and right chambers of the hydraulic cylinder, respectively; $p_L = p_1 - p_2$ is the pressure difference; A_d is the pressurized area of the hydraulic cylinder; B is the coefficient of the kinematic viscous damping; and F_L is the sum of the nonlinear interferences including the kinematic friction.

If the external leakage factor of the hydraulic system is ignored, the dynamic equation of the pressure in the left and right chambers of the hydraulic cylinder is:

$$\begin{cases} \dot{p}_1 = \dfrac{\beta_e}{V_1}\left(-A_d\dot{x}_p - C_t p_L + Q_1\right) \\ \dot{p}_2 = \dfrac{\beta_e}{V_2}\left(A_d\dot{x}_p + C_t p_L - Q_2\right) \end{cases} \tag{2}$$

where β_e is the effective volumetric bulk modulus of hydraulic oil; $V_1 = V_{01} + A_d x_p$ is the volume of the left chamber; V_{01} is the initial volume of the left chamber; $V_2 = V_{02} - A_d x_p$ is the volume of the right chamber; V_{02} is the initial volume of the right chamber, and $V_{01} = V_{02} = V_0$; Q_1 is the supply flow rate of hydraulic cylinder; Q_2 is the return flow rate of hydraulic cylinder; and C_t is the total internal leakage coefficient. According to $p_L = p_1 - p_2$, the following equation can be obtained:

$$\dot{p}_L = -\frac{(V_1+V_2)A_d\beta_e}{V_1V_2}\dot{x}_p - \frac{(V_1+V_2)C_t\beta_e}{V_1V_2}p_L + \frac{(Q_1V_2+Q_2V_1)\beta_e}{V_1V_2} \tag{3}$$

The equations of flow rates are as follows:

$$\begin{cases} Q_1 = K_e u\left[s(u)\sqrt{p_s - p_1} + s(-u)\sqrt{p_1 - p_r}\right] \\ Q_2 = K_e u\left[s(u)\sqrt{p_2 - p_r} + s(-u)\sqrt{p_s - p_2}\right] \end{cases} \tag{4}$$

where K_e represents the total flow gain of the servo valve; p_s represents the supply pressure; p_r represents the return pressure; and u represents the control voltage. The function $s(u)$ is defined as follows:

$$s(u) = \begin{cases} 1, & u \geq 0 \\ 0, & u < 0 \end{cases} \tag{5}$$

The state variables of the electro-hydraulic position servo system are defined as $\boldsymbol{x} = \left[x_1\ x_2\ x_3\right]^{\mathrm{T}} = \left[x_p\ \dot{x}_p\ p_L\right]^{\mathrm{T}}$. Then, the third-order state space expression of the entire system can be obtained as:

$$\begin{cases} \dot{x}_1 = x_2 \\ \dot{x}_2 = \dfrac{1}{m}\left(A_d x_3 - Bx_2 - F_L\right) \\ \dot{x}_3 = f_x + g_x u \\ y = x_1 \end{cases} \tag{6}$$

where F_L is a bounded function. The definitions of f_x and g_x are as follows:

$$\begin{cases} R_1 = s(u)\sqrt{p_s - p_1} + s(-u)\sqrt{p_1 - p_r} \\ R_2 = s(u)\sqrt{p_2 - p_r} + s(-u)\sqrt{p_s - p_2} \\ f_x = -\dfrac{(V_1+V_2)A_d\beta_e}{V_1V_2}x_2 - \dfrac{(V_1+V_2)C_t\beta_e}{V_1V_2}x_3 \\ g_x = \dfrac{\beta_e K_e(R_1V_2 + R_2V_1)}{V_1V_2} \end{cases} \tag{7}$$

3. Controller design

The controller block diagram is shown in Figure 2.

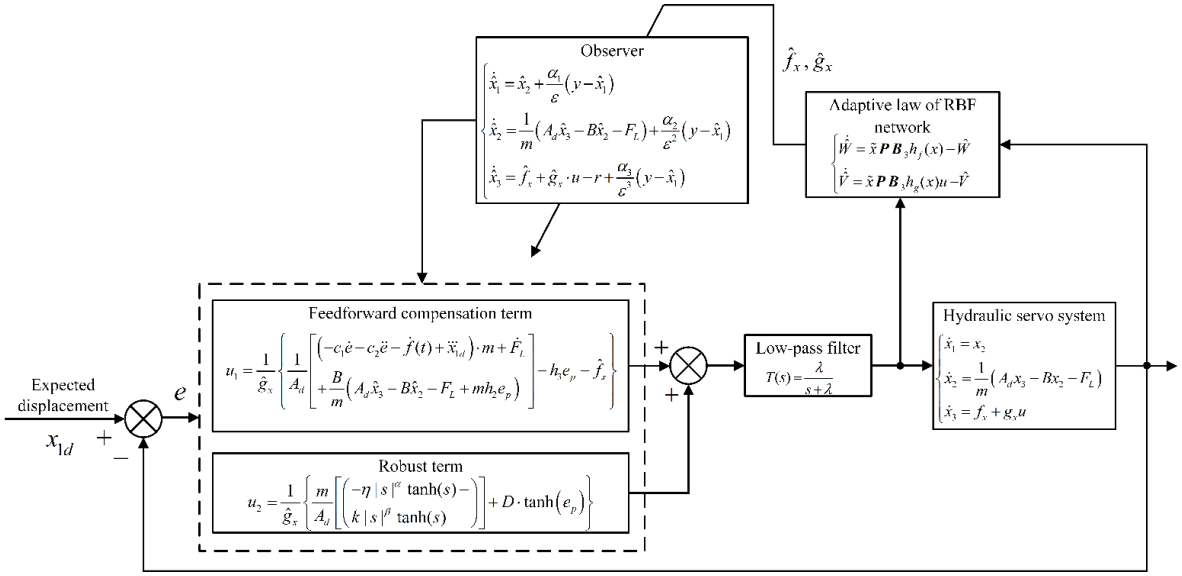

Figure 2. Controller block diagram.

As shown in Figure 2, the system takes the expected displacement command of the hydraulic cylinder piston as input. The initial control signal from the sliding mode controller is smoothed using a low-pass filter to mitigate chattering caused by high-frequency switching. Then, the servo valve drives the hydraulic cylinder to control the displacement of the piston. Concurrently, the RBF neural network adaptive observer performs real-time estimation of the system's displacement, velocity, and nonlinear components. These estimated parameters are subsequently fed back into the sliding mode controller to dynamically compensate for model uncertainties and external disturbances. The neural network is updated by an adaptive law designed based on the Lyapunov function, thus forming a complete closed-loop framework that ensures high precision, fast response, and strong robustness of the system.

3.1. RBF adaptive state observer design

In practical applications, complex dynamic problems occur, including nonlinear disturbances, parameter uncertainties, and unmodeled dynamic behaviors. These problems may lead to system performance degradation in application scenarios requiring high accuracy and fast response, such as increased steady-state error and reduced stability. The state observer can monitor the state of the system in real time. By designing suitable observers, the displacement and velocity of the actuator can be estimated online, providing accurate observation of these signals that are difficult to measure directly.

In order to reduce the abrupt change or chattering in the controller, the RBF neural network is used to approximate the nonlinear terms f_x and g_x. The RBF neural network is mainly composed of the input layer, the hidden layer, and the output layer, and its basic structure is shown in Figure 3.

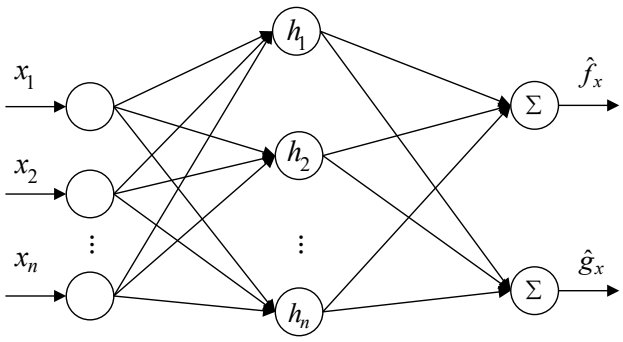

Figure 3. RBF neural network structure.

Using RBF universal approximation characteristics to approximate 1 and 2, the network algorithm is:

$$h_j = \exp\left(-\frac{\left\|x - c_j\right\|^2}{2b_j^2}\right) \tag{8}$$

$$\begin{cases} f_x = \boldsymbol{W}^{*\mathrm{T}}\boldsymbol{h}_{\boldsymbol{f}}(x) + \varepsilon_1 \\ g_x = \boldsymbol{V}^{*\mathrm{T}}\boldsymbol{h}_{\boldsymbol{g}}(x) + \varepsilon_2 \end{cases} \tag{9}$$

where x is the input of the network, j is the node of the hidden layer, $\boldsymbol{W}^*$ and $\boldsymbol{V}^*$ are the ideal weights of the network, and $\varepsilon_1, \varepsilon_2$ is the approximation error of the network; all of which are bounded real numbers.

If the network input is set to $\boldsymbol{x} = \left[x_1\ x_2\ x_3\ u\right]$, the network output is:

$$\begin{cases} \hat{f}_x = \hat{\boldsymbol{W}}^{\mathrm{T}}\boldsymbol{h}_{\boldsymbol{f}}(x) \\ \hat{g}_x = \hat{\boldsymbol{V}}^{\mathrm{T}}\boldsymbol{h}_{\boldsymbol{g}}(x) \end{cases} \tag{10}$$

where $\hat{\boldsymbol{w}}$ and $\hat{\boldsymbol{v}}$ are estimates of neural network weights, and the weight update rule is provided in Section 4.

The observer is designed as follows:

$$\begin{cases} \dot{\hat{x}}_1 = \hat{x}_2 + \dfrac{\alpha_1}{\varepsilon}\left(y - \hat{x}_1\right) \\ \dot{\hat{x}}_2 = \dfrac{1}{m}\left(A_d\hat{x}_3 - B\hat{x}_2 - F_L\right) + \dfrac{\alpha_2}{\varepsilon^2}\left(y - \hat{x}_1\right) \\ \dot{\hat{x}}_3 = \hat{f}_x + \hat{g}_x \cdot u - r + \dfrac{\alpha_3}{\varepsilon^3}\left(y - \hat{x}_1\right) \end{cases} \tag{11}$$

Where $r = D \cdot \tanh(e_p)$ is the robust term, D is the parameter to be designed, tanh is an hyperbolic tangent function, $e_p = x_1 - \hat{x}_1$ is the position observation error, $\hat{x}_1, \hat{x}_2, \hat{x}_3$ are observer states, $0 < \varepsilon << 1$, and α_1, α_2, and α_3 are positive real numbers.

Define $\tilde{\boldsymbol{x}} = \boldsymbol{x} - \hat{\boldsymbol{x}}, \tilde{\boldsymbol{W}} = \hat{\boldsymbol{W}} - \boldsymbol{W}^*, \tilde{\boldsymbol{V}} = \hat{\boldsymbol{V}} - \boldsymbol{V}^*$, let $h_1 = \frac{\alpha_1}{\varepsilon}, h_2 = \frac{\alpha_2}{\varepsilon^2}, h_3 = \frac{\alpha_3}{\varepsilon^3}$, then the equation of state for the estimation error is:

$$\begin{cases} \dot{\tilde{x}}_1 = -h_1\tilde{x}_1 + \tilde{x}_2 \\ \dot{\tilde{x}}_2 = -h_2\tilde{x}_1 + \frac{1}{m}\left(A_d\tilde{x}_3 - B\tilde{x}_2\right) \\ \dot{\tilde{x}}_3 = -h_3\tilde{x}_1 - \tilde{\boldsymbol{W}}^T\boldsymbol{h}_{\boldsymbol{f}}(x) + \varepsilon_1 \\ \qquad -\tilde{\boldsymbol{V}}^T\boldsymbol{h}_{\boldsymbol{g}}(x)u + \varepsilon_2 + r \end{cases} \tag{12}$$

Let $\boldsymbol{A} = \begin{pmatrix} -h_1 & 1 & 0 \\ -h_2 & 0 & 1 \\ -h_3 & 0 & 0 \end{pmatrix}, \boldsymbol{H} = \begin{bmatrix} 0 \\ \frac{A_d - m}{m}\tilde{x}_3 - \frac{B}{m}\tilde{x}_2 \\ -\tilde{\boldsymbol{W}}^{\mathrm{T}}\boldsymbol{h}_f(x) + \varepsilon_1 - \tilde{\boldsymbol{V}}^{\mathrm{T}}\boldsymbol{h}_g(x)u + \varepsilon_2 + r \end{bmatrix}$, then the equation of state for the estimation error can be simplified as follows:

$$\dot{\tilde{\boldsymbol{x}}} = \boldsymbol{A}\tilde{\boldsymbol{x}} + \boldsymbol{H} \tag{13}$$

When $h_j > 0$ in matrix $\boldsymbol{A}$, $\boldsymbol{A}$ is a Hurwitz matrix, i.e., the eigenvalues of $\boldsymbol{A}$ are negative, then there exists a real symmetric positive definite matrix $\boldsymbol{P}$ and a positive definite matrix $\boldsymbol{Q}$ satisfying the following equations:

$$\boldsymbol{A}^{\mathrm{T}}\boldsymbol{P} + \boldsymbol{P}\boldsymbol{A} + \boldsymbol{Q} = 0 \tag{14}$$

3.2. Sliding mode controller design

Define x_{1d} as ideal tracking signal and $e = \hat{x}_1 - x_{1d}$ as the position tracking error of system, and the sliding mode surface can be designed as:

$$s = c_1 e + c_2 \dot{e} + \ddot{e} + f(t) \tag{15}$$

where c_1 and c_2 are constants greater than 0, designed to satisfy the Hurwitz condition. $f(t)$ is an auxiliary function designed to enable the system to achieve global sliding mode, whose characteristics satisfy the following conditions: $f(t)$ is differentiable of the first order; when $t \to \infty$, $f(t) \to 0$; and $f(0) = c_1 e(0) + c_2 \dot{e}(0) + \ddot{e}(0)$.

$f(t)$ is designed as follows:

$$f(t) = f(0) \cdot e^{-at} \tag{16}$$

Taking the derivative of Eq (15), it can be obtained as follows:

$$\begin{aligned}\dot{s} &= c_1\dot{e} + c_2\ddot{e} + \dddot{e} + \dot{f}(t) \\ &= c_1\dot{e} + c_2\ddot{e} + \frac{1}{m}\left(A_d\dot{\hat{x}}_3 - B\dot{\hat{x}}_2 - \dot{F}_L\right) - \dddot{x}_{1d} + \dot{f}(t) \\ &= \frac{1}{m}\begin{Bmatrix} A_d\left(\hat{f}_x + \hat{g}_x\cdot u - r + h_3e_p\right) - \dot{F}_L + \\ h_2e_p - B\left[\frac{1}{m}\left(A_d\hat{x}_3 - B\hat{x}_2 - F_L\right)\right]\end{Bmatrix} + c_1\dot{e} + c_2\ddot{e} - \dddot{x}_{1d} + \dot{f}(t)\end{aligned} \tag{17}$$

To mitigate the chattering phenomenon associated with the sign function in conventional sliding mode reaching laws, while simultaneously preserving the rapid convergence characteristic during large error conditions and ensuring steady-state precision in the vicinity of small errors, a sliding mode reaching law integrating a power term with a hyperbolic tangent function is proposed, as expressed below:

$$\dot{s} = -\eta\,|s|^{\alpha}\,\tanh(s) - k\,|s|^{\beta}\,\tanh(s) \tag{18}$$

where η and k are both parameters to be designed greater than 0, while α and β satisfy $0<\alpha<1<\beta$. When the state of the system is far away from the sliding mode surface, the approaching speed is adjusted by the power term $|s|^{\alpha}$ to realize fast convergence; when the state of the system is close to the sliding mode surface, the approaching accuracy is controlled by the power term $|s|^{\beta}$ to avoid high frequency chattering. The hyperbolic tangent function is employed as a substitute for the sign function to achieve continuous smooth control, so that the dynamic response and steady-state tracking performance are optimized while suppressing chattering.

According to Eqs (17) and (18), the sliding mode control law based on the RBF adaptive observer can be designed as follows:

$$u = \frac{1}{\hat{g}_x}\begin{Bmatrix} \frac{1}{A_d}\left[\begin{pmatrix} -\eta\,|s|^{\alpha}\,\tanh(s) - k\,|s|^{\beta}\,\tanh(s) \\ -c_1\dot{e} - c_2\ddot{e} - \dot{f}(t) + \dddot{x}_{1d}\end{pmatrix}\cdot m + \dot{F}_L + \frac{B}{m}\begin{pmatrix} A_d\hat{x}_3 - B\hat{x}_2 \\ -F_L + mh_2e_p\end{pmatrix}\right] \\ -h_3e_p - \hat{f}_x + r\end{Bmatrix} \tag{19}$$

where $k>0, \eta>0$.

In the design of sliding mode controllers, as the system state nears the sliding surface, the rapid switching of the control law often induces sudden variations in the control gain along the sliding surface. This phenomenon, known as chattering, can substantially impair overall control performance. To mitigate chattering caused by sliding mode gains, a composite control strategy combining sliding mode variable structure control with filtering can be employed. This effectively attenuates chattering signals, ensuring the smooth continuity of the system controller and providing smoother position and velocity responses for the system model. Introducing a low-pass filter as shown in Eq (20) to smooth the controller's switching control quantities can significantly suppress oscillation while maintaining system robustness.

$$T(s) = \frac{\lambda}{s+\lambda} \tag{20}$$

where λ is the bandwidth of the filter.

The time-domain differential equation for the filter is：

$$\dot{y}_f(t) + \lambda y_f(t) = \lambda u(t) \tag{21}$$

where $u(t)$ is the signal before filtering, and $y_f(t)$ is the filtered output signal.

From Eq (19), it follows that u is continuously differentiable. Defining the filtering error as $e_f(t) = u(t) - y_f(t)$, differentiating it and substituting into Eq (21) yields the following expression:

$$\dot{e}_f(t) = \dot{u}(t) - \lambda e_f(t) \tag{22}$$

The solution to the differential equation shown in (22) is:

$$e(t) = e(0)e^{-\lambda t} + \int_0^t e^{-\lambda(t-\tau)}\dot{u}(\tau)d\tau \tag{23}$$

When the derivative of the input signal is bounded, the following equation holds:

$$e(t) \le e(0)e^{-\lambda t} + \frac{L}{\lambda}(1 - e^{-\lambda t}) \tag{24}$$

When $t \to \infty$, $\lim_{t\to\infty} |e(t)| \le \frac{L}{\lambda}$, so the filtering error ultimately converges to a bounded value.

4. System stability analysis

The Lyapunov function for the sliding mode control is taken as:

$$V_s = \frac{1}{2}s^2 \tag{25}$$

Differentiating both sides of Eq (25) yields:

$$\begin{aligned} \dot{V}_s &= s\dot{s} \\ &= s\left\{\frac{1}{m}\begin{bmatrix} A_d\left(\hat{f}_x + \hat{g}_x \cdot u - r + h_3 e_p\right) - \dot{F}_L - \\ B\left(\frac{1}{m}\left(A_d\hat{x}_3 - B\hat{x}_2 - F_L\right) + h_2 e_p\right) \end{bmatrix} - \dddot{x}_{1d} + c_1\ddot{e} + c_2\dddot{e} + \dot{f}(t)\right\} \end{aligned} \tag{26}$$

Substituting the control law u into Eq (26) yields:

$$\dot{V}_s = -\eta s|s|^{\alpha}\tanh(s) - k s|s|^{\beta}\tanh(s) \tag{27}$$

Because $k>0,\eta>0$, when $s>0$, then $\dot{V}_s=-(\eta s^{\alpha+1}+ks^{\beta+1})\tanh(s)$; at this moment, $\tanh(s)>0$; therefore, there is $\dot{V}_s\le 0$. When $s\le 0$, then $\tanh(s)\le 0$, $s|s|^{\alpha}\le 0$, and $s|s|^{\beta}\le 0$; therefore, there still is $\dot{V}_s\le 0$.

Take the Lyapunov function of the closed-loop system as:

$$V=V_s+V_o \tag{28}$$

where

$$V_o=\frac{1}{2}\tilde{\boldsymbol{x}}^{\mathrm{T}}\boldsymbol{P}\tilde{\boldsymbol{x}}+\frac{1}{2}\tilde{\boldsymbol{W}}^{\mathrm{T}}\tilde{\boldsymbol{W}}+\frac{1}{2}\tilde{\boldsymbol{V}}^{\mathrm{T}}\tilde{\boldsymbol{V}} \tag{29}$$

Clearly, Eq (29) is a positive definite function. Substituting Eq (13) into its time derivative of Eq (29) yields:

$$\begin{aligned}\dot{V}_o&=\tilde{\boldsymbol{x}}^{\mathrm{T}}\boldsymbol{P}\dot{\tilde{\boldsymbol{x}}}+\tilde{\boldsymbol{W}}^{\mathrm{T}}\dot{\tilde{\boldsymbol{W}}}+\tilde{\boldsymbol{V}}^{\mathrm{T}}\dot{\tilde{\boldsymbol{V}}}\\&=\tilde{\boldsymbol{x}}^{\mathrm{T}}\boldsymbol{P}\boldsymbol{A}\tilde{\boldsymbol{x}}+\tilde{\boldsymbol{x}}^{\mathrm{T}}\boldsymbol{P}\boldsymbol{H}+\tilde{\boldsymbol{W}}^{\mathrm{T}}\dot{\tilde{\boldsymbol{W}}}+\tilde{\boldsymbol{V}}^{\mathrm{T}}\dot{\tilde{\boldsymbol{V}}}\\&=-\frac{\lambda_{\min}(\boldsymbol{Q})}{2}\|\tilde{\boldsymbol{x}}\|^2-\frac{B}{m}\tilde{\boldsymbol{x}}^{\mathrm{T}}\boldsymbol{P}\boldsymbol{B}_1\tilde{x}_2-\frac{m-A_d}{m}\tilde{\boldsymbol{x}}^{\mathrm{T}}\boldsymbol{P}\boldsymbol{B}_2\tilde{x}_3+\tilde{\boldsymbol{x}}^{\mathrm{T}}\boldsymbol{P}\boldsymbol{B}_3\left[-\tilde{\boldsymbol{W}}^{\mathrm{T}}\boldsymbol{h}_f(x)\right.\\&\quad\left.-\tilde{\boldsymbol{V}}^{\mathrm{T}}\boldsymbol{h}_g(x)u+c\right]+\tilde{\boldsymbol{W}}^{\mathrm{T}}\dot{\tilde{\boldsymbol{W}}}+\tilde{\boldsymbol{V}}^{\mathrm{T}}\dot{\tilde{\boldsymbol{V}}}\end{aligned} \tag{30}$$

where $\boldsymbol{B}_1^{\mathrm{T}}=[0\ 1\ 0]$, $\boldsymbol{B}_2^{\mathrm{T}}=[0\ 1\ 0]$, $\boldsymbol{B}_3^{\mathrm{T}}=[0\ 0\ 1]$, and $c=\varepsilon_1+\varepsilon_2+r$. Define $\lambda_{\min}$ and $\lambda_{\max}$ as the minimum and maximum eigenvalues of the matrix, respectively. The adaptive law for neural network weights is:

$$\begin{cases}\dot{\hat{\boldsymbol{W}}}=\tilde{\boldsymbol{x}}\boldsymbol{P}\boldsymbol{B}_3\boldsymbol{h}_f(x)-\hat{\boldsymbol{W}}\\\dot{\hat{\boldsymbol{V}}}=\tilde{\boldsymbol{x}}\boldsymbol{P}\boldsymbol{B}_3\boldsymbol{h}_g(x)u-\hat{\boldsymbol{V}}\end{cases} \tag{31}$$

Substituting Eq (31) into (30) and expanding the right-hand side yields:

$$\begin{aligned}\dot{V}_{\mathrm{o}}&=-\frac{\lambda_{\min}(\boldsymbol{Q})}{2}\|\tilde{\boldsymbol{x}}\|^2-\frac{B}{m}\tilde{\boldsymbol{x}}^{\mathrm{T}}\boldsymbol{P}\boldsymbol{B}_1\tilde{x}_2-\frac{m-A_d}{m}\tilde{\boldsymbol{x}}^{\mathrm{T}}\boldsymbol{P}\boldsymbol{B}_2\tilde{x}_3+c\tilde{\boldsymbol{x}}^{\mathrm{T}}\boldsymbol{P}\boldsymbol{B}_3-\tilde{\boldsymbol{W}}^{\mathrm{T}}\hat{\boldsymbol{W}}-\tilde{\boldsymbol{V}}^{\mathrm{T}}\hat{\boldsymbol{V}}\\&\le-\frac{\lambda_{\min}(\boldsymbol{Q})}{2}\|\tilde{\boldsymbol{x}}\|^2-\frac{B}{m}\|\boldsymbol{P}\boldsymbol{B}_1\|\|\tilde{\boldsymbol{x}}\|^2-\frac{m-A_d}{m}\|\boldsymbol{P}\boldsymbol{B}_2\|\|\tilde{\boldsymbol{x}}\|^2+\frac{1}{2}\|\tilde{\boldsymbol{x}}\|^2+\frac{1}{2}c^2\|\boldsymbol{P}\boldsymbol{B}_3\|^2\\&\quad-\frac{1}{2}\|\tilde{\boldsymbol{W}}\|^2-\frac{1}{2}\|\tilde{\boldsymbol{V}}\|^2+\frac{1}{2}\|\boldsymbol{W}^*\|^2+\frac{1}{2}\|\boldsymbol{V}^*\|^2\\&=-\boldsymbol{\zeta}^{\mathrm{T}}\boldsymbol{\Gamma}\boldsymbol{\zeta}-\frac{1}{2}\|\tilde{\boldsymbol{W}}\|^2-\frac{1}{2}\|\tilde{\boldsymbol{V}}\|^2+\gamma\end{aligned} \tag{32}$$

Define the parameters as follows:

$$\begin{cases} \boldsymbol{\zeta}^{\mathrm{T}} = \left[|\tilde{\boldsymbol{x}}|, |\tilde{\boldsymbol{x}}|, |\tilde{\boldsymbol{x}}|, |\tilde{\boldsymbol{x}}| \right] \\ \boldsymbol{\Gamma} = \mathrm{diag}\left[\tau_1, \tau_2, \tau_3, \tau_4 \right] \\ \gamma = \dfrac{1}{2}\left\| \boldsymbol{W}^* \right\|^2 + \dfrac{1}{2}\left\| \boldsymbol{V}^* \right\|^2 + \dfrac{1}{2}c^2 \left\| \boldsymbol{P}\boldsymbol{B}_3 \right\|^2 \end{cases} \tag{33}$$

where $\tau_1 = \dfrac{\lambda_{\min}(\boldsymbol{Q})}{2}, \tau_2 = \dfrac{B}{m}, \tau_3 = \dfrac{m - A_d}{m}, \tau_4 = \dfrac{1}{2}$. Selecting an appropriate matrix $\boldsymbol{Q}$ ensures that $\boldsymbol{\Gamma}$ is positive definite, and $\dot{V}_o$ can be obtained as:

$$\begin{aligned} \dot{V}_o &\le -\lambda_{\min}(\boldsymbol{\Gamma})\left\| \tilde{\boldsymbol{x}} \right\|^2 - \frac{1}{2}\left\| \tilde{\boldsymbol{W}} \right\|^2 - \frac{1}{2}\left\| \tilde{\boldsymbol{V}} \right\|^2 + \gamma \\ &\le -\frac{\lambda_{\min}(\boldsymbol{\Gamma})}{\lambda_{\max}(\boldsymbol{P})}\left\| \tilde{\boldsymbol{x}} \right\|^2 - \frac{1}{2}\left\| \tilde{\boldsymbol{W}} \right\|^2 - \frac{1}{2}\left\| \tilde{\boldsymbol{V}} \right\|^2 + \gamma \\ &\le -\left[\frac{\lambda_{\min}(\boldsymbol{\Gamma})}{\lambda_{\max}(\boldsymbol{P})}, \frac{1}{2} \right]_{\min} \cdot V_{\mathrm{o}} + \gamma \end{aligned} \tag{34}$$

Let $\boldsymbol{\delta} = \left[\dfrac{\lambda_{\min}(\boldsymbol{\Gamma})}{\lambda_{\max}(\boldsymbol{P})}, \dfrac{1}{2} \right]_{\min}$. For the differential inequality (34), the solution for any $t \ge 0$ is:

$$V_o(t) \le V(0)\,\mathrm{e}^{-\delta t} + \frac{\gamma}{\boldsymbol{\delta}}(1 - \mathrm{e}^{-\delta t}) \tag{35}$$

From Eqs (27) and (35), it can be seen that the system can achieve bounded stability.

5. Simulation experiment analysis

The relevant parameters adopted by the model are shown in Table 1. To quantitatively assess the dynamic performance of the proposed control strategy, a mathematical model of the electro-hydraulic position servo system was developed within the Matlab/Simulink simulation environment, utilizing the parameters provided in Table 1. Subsequently, simulation analyses were conducted.

When setting the gain parameters of the observer, it is only necessary to ensure that the system matrix $\boldsymbol{A}$ of the observer's estimated error state equation satisfies the Hurwitz condition. Subsequently, manual fine-tuning can be performed based on engineering experience under these circumstances. When configuring neural network parameters, the model's observable values are selected as the input vector. The choice of center vector $\boldsymbol{c}$ should correspond to the input vector's range, meaning its numerical interval must be at least greater than that of the input vector. The width b of the Gauss-Kohler function correlates with the neural network's mapping capability for the input vector; typically, its value is set to a moderate level during debugging. During simulation debugging, a large initial value is assigned to the sliding surface parameter c_1 and a small initial value to c_2 (while satisfying the Hurwitz condition). Gradual fine-tuning is based on tracking performance. Sliding approach law parameters η and k are incremented proportionally until oscillation subsides. Finally, α and β are adjusted to ensure that α is much smaller than β, to balance convergence speed and steady-state accuracy. The controller exhibits low sensitivity to the filter parameter λ, which

can typically be selected using common empirical values. The final control parameters for the RBF neural network-based adaptive observer sliding mode controller (RBFSMC) are presented in Table 2.

Table 1. Parameters of the electro-hydraulic position servo system.

Name	Symbol	Numerical value
Effective area of the symmetrical cylinder	A_d	1.26×10^{-3} m^2
Equivalent load mass	m	300 kg
Oil supply pressure	p_s	1×10^7 Pa
Return oil pressure	p_r	0
Hydraulic oil volume elastic modulus	β_e	6.09×10^8 Pa
Valve gain coefficient	K_e	3.81×10^{-8} m$^3\cdot$(s$\cdot$V$\cdot\sqrt{\text{Pa}}$)$^{-1}$
Initial volume of the hydraulic cylinder	V_0	2.03×10^{-3} m^3
Hydraulic cylinder internal leakage coefficient	C_t	5×10^{-12} m$^5\cdot$(N$\cdot$s)$^{-1}$
Kinematic viscosity damping coefficient	B	3×10^3 N$\cdot$(m/s)$^{-1}$

Table 2. Parameters of the RBFSMC controller.

Parameters	Values	Parameters	Values
c_1	4×10^4	D	0.2
c_2	10	α_1	185
b	10	α_2	200
λ	25	α_3	10^{14}
ε	0.001	a	100
η	400	k	1

To assess the efficacy of the control strategy introduced in this study, simulations were conducted comparing the proposed controller with a particle swarm optimization-based PID controller (PSOPID) [35] and an ASMC controller [36], the latter employing a parameter adaptation law derived from the Lyapunov function associated with sliding mode control. These controllers were evaluated under three distinct reference signals: Reference signal 1: $x_{1d}=0.8$; Reference signal 2: $x_{1d}=\sin(\pi t)(1-e^{-t})$; Reference signal 3: $x_{1d}=0.1\sin(\pi t/2-\pi/6)+0.05$). Their respective tracking errors were analyzed and compared. During the evaluation process, three key performance indicators were used to assess the tracking quality of the control system: the average tracking error μ, the maximum steady-state error M_e, and the standard deviation of the tracking error σ. These are defined as follows:

$$\begin{cases} \mu=\dfrac{1}{N}\sum\limits_{i=1}^{N}\left|e(i)\right| \\ M_{\mathrm{e}}=\max\limits_{i=1,2,\cdots,n}\left\{\left|e(i)\right|\right\} \\ \sigma=\sqrt{\dfrac{1}{N}\sum\limits_{i=1}^{N}\left(\left|e(i)\right|-\mu\right)^2} \end{cases} \tag{36}$$

In the simulation, to verify the controller's robustness, disturbances were applied under three reference signals at $-0.1\sin(x_1)$, $-0.2\sin(x_1x_2)$, and $-0.25\sin(x_1x_2+0.5t)e^{-0.1x_1}$. At $t=3$, the equivalent load m is suddenly increased to 1.2 times its original value, while parameters C_t, K_e, and β are reduced to 85% of their original values, with this state persisting for 3 s.

Figure 4 illustrates the tracking performances of the three controllers in response to reference signal 1 (a step input), and Table 3 provides a comparative analysis of their transient response characteristics.

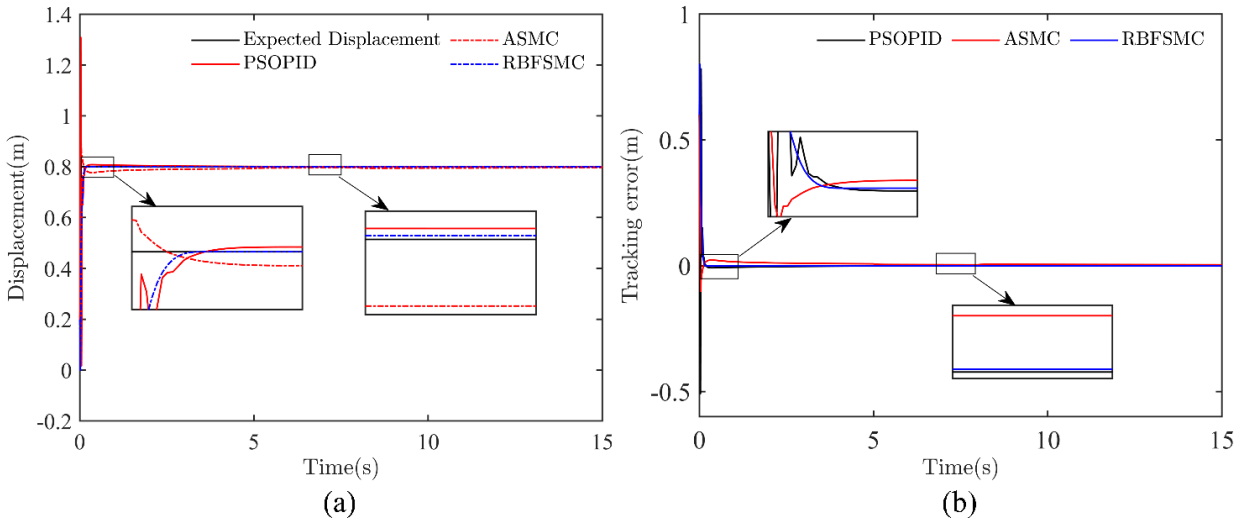

Figure 4. Tracking performances of the three controllers under reference signal 1.

Table 3. Simulation performance indexes under reference signal 1.

Controllers	μ	M_e	σ	Settling time (s)	Overshoot (%)
PSOPID	3.89×10^{-3}	1.06×10^{-3}	3.53×10^{-2}	0.165	63.50
ASMC	3.30×10^{-3}	2.39×10^{-3}	2.22×10^{-2}	4.51	12.73
RBFSMC	2.82×10^{-3}	7.71×10^{-4}	3.81×10^{-2}	0.09	0

As illustrated in Figure 4, the displacement response curve corresponding to the RBFSMC controller demonstrates the most rapid rise time and the least overshoot. Furthermore, its steady-state error remains consistently lower compared to those observed in the PSOPID and ASMC controllers. This demonstrates superior transient performance and robustness. In conjunction with the quantitative data presented in Table 3, the RBFSMC controller demonstrates an average error reduction of approximately 27.51% relative to the PSOPID controller and 14.55% relative to the ASMC controller. These findings further substantiate the dual benefits of the RBFSMC controller in terms of both accuracy and response speed.

The tracking performances of the three controllers under reference signal 2 are compared in Figure 5, while the observation performance of the observer is compared in Figure 6. To quantitatively evaluate the controllers' performance, their performance metrics were calculated using the performance index formula, as shown in Table 4.

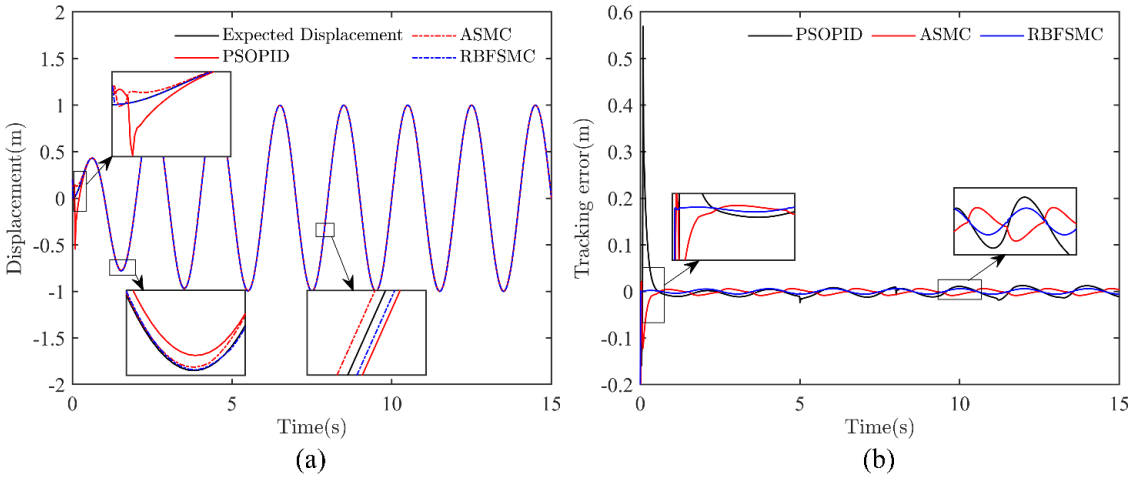

Figure 5. Tacking performances of three controllers under reference signal 2.

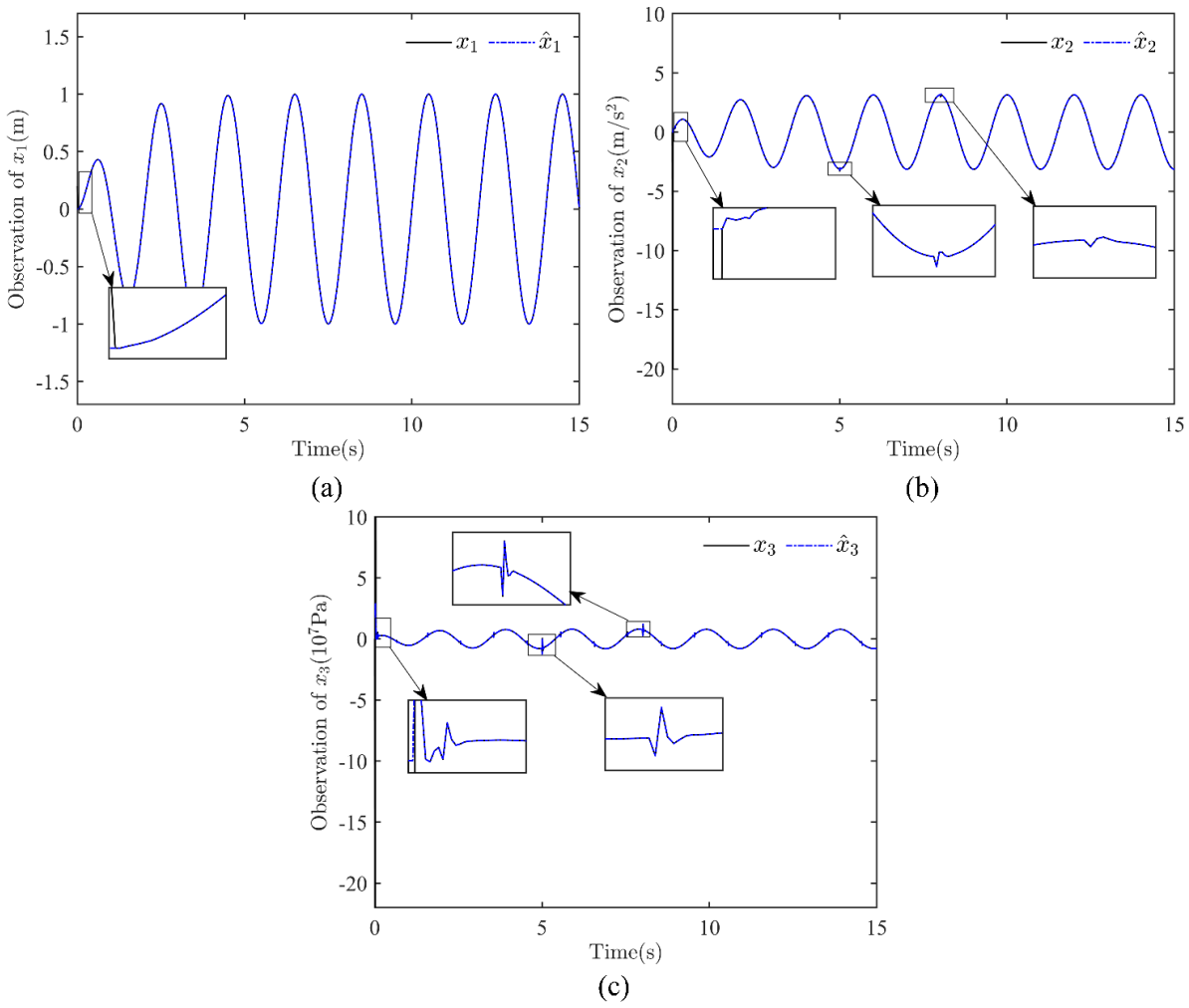

Figure 6. Observer performances under reference signal 2.

Table 4. Simulation performance indexes under reference signal 2.

Controllers	μ	M_e	σ
PSOPID	5.33×10^{-3}	1.93×10^{-2}	2.54×10^{-2}
ASMC	5.13×10^{-3}	1.19×10^{-2}	7.86×10^{-3}
RBFSMC	3.7×10^{-3}	7.34×10^{-3}	5.37×10^{-3}

As shown in Figure 5, the RBFSMC controller demonstrates superior response speed and steady-state error compared to the other two controllers. It also exhibits minimal tracking error fluctuations during parameter abrupt changes, indicating excellent robustness. The observation performance of the three state variables in Figure 6 demonstrates that the designed neural network-based adaptive observer accurately estimates the model state under reference signal 2. It exhibits fast response speed and maintains continuous observation even during sudden parameter changes, indicating excellent observation performance. Table 4 demonstrates that, in comparison to the PSOPID and ASMC controllers, the RBFSMC controller attains superior performance across all three evaluated metrics. Specifically, its mean error is decreased by 30.58% relative to the PSOPID controller and by 27.87% relative to the ASMC controller.

The tracking performance comparisons of the three controllers under reference signal 3 are shown in Figure 7. The observation performance comparisons of the observer are shown in Figure 8. The performance metrics comparisons of the three controllers are shown in Table 5.

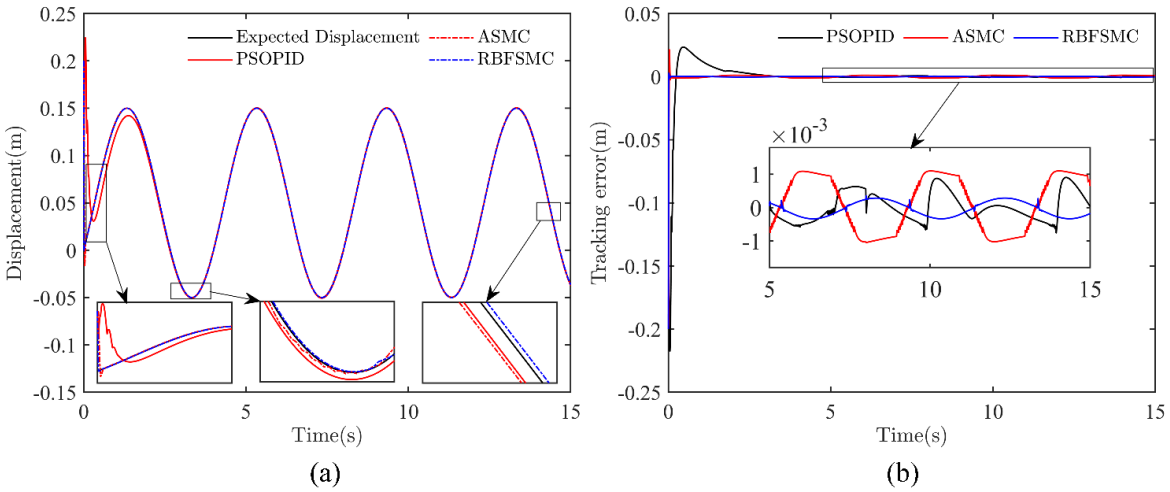

Figure 7. Tracking performances of three controllers under reference signal 3.

Table 5. Simulation performance indexes under reference signal 3.

Controllers	μ	M_e	σ
PSOPID	3.50×10^{-3}	9.04×10^{-4}	1.63×10^{-2}
ASMC	1.10×10^{-3}	1.10×10^{-3}	7.30×10^{-3}
RBFSMC	3.43×10^{-4}	3.53×10^{-4}	5.16×10^{-3}

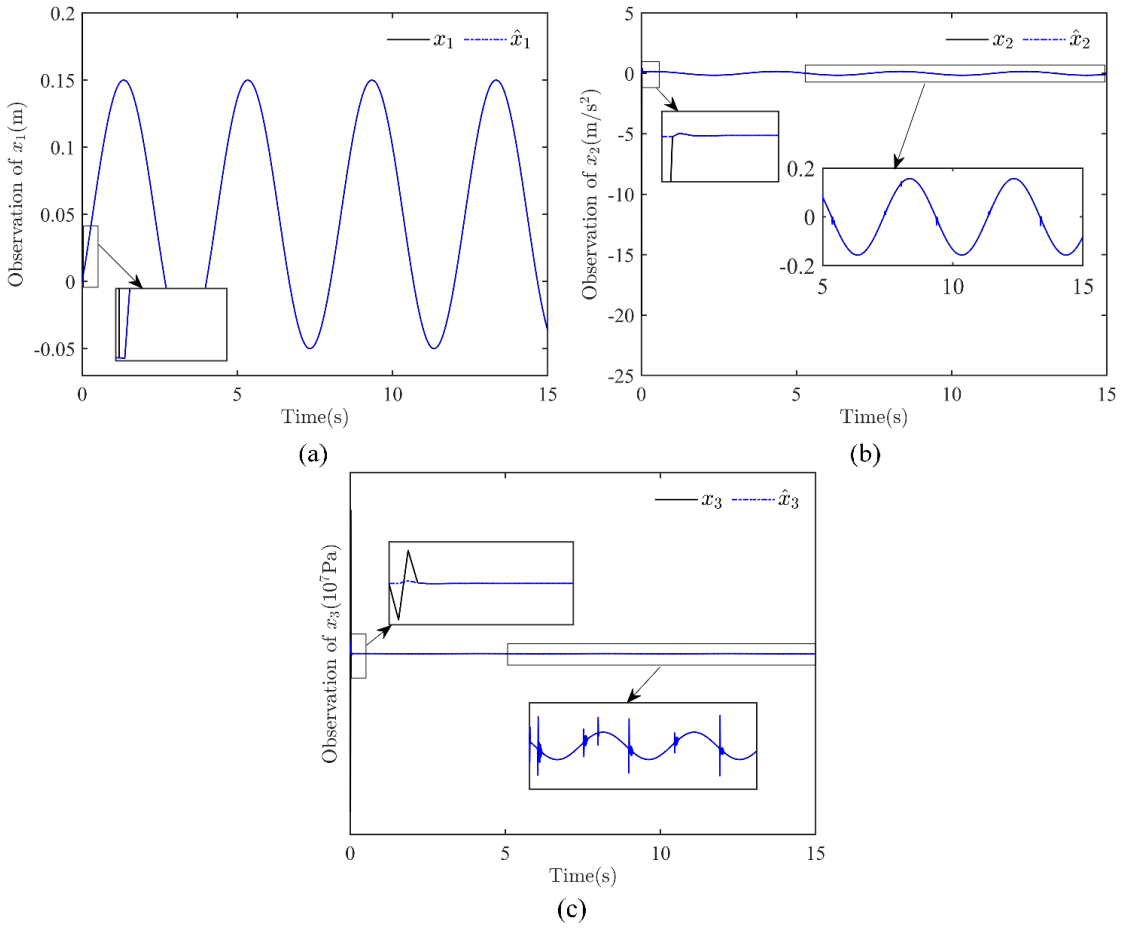

Figure 8. Observer performances under reference signal 3.

As illustrated in the tracking performance presented in Figure 7, the RBFSMC controller still exhibits the fastest response speed and steady-state accuracy under reference signal 3 compared to the other two controllers. As shown in the tracking performance of the three state variables in Figure 8, the designed neural network observer accurately estimates the model's state variables under reference signal 3. As indicated in Table 5, the RBFSMC controller consistently exhibits superior performance across all three evaluated metrics when compared to the PSOPID and ASMC controllers. Specifically, it achieves an average error reduction of 90.2% relative to the PSOPID controller and 68.82% relative to the ASMC controller.

Simulation outcomes across three distinct reference signals indicate that the PSOPID and ASMC controllers display substantial tracking errors, prolonged convergence durations, and a marked susceptibility to instability in response to sudden parameter variations, thereby reflecting inadequate disturbance rejection capabilities. In contrast, the RBFSMC controller not only achieves minimal tracking errors but also converges rapidly within an extremely short timeframe. It delivers stable tracking performance and higher steady-state accuracy. Across the three comprehensive performance metrics—maximum tracking error, average tracking error, and standard deviation of tracking error—RBFSMC demonstrates a clear advantage. This suggests that the controller not only provides precise estimation of the system state within the hydraulic system but also successfully achieves a balance between dynamic response speed and steady-state accuracy, demonstrating strong robustness.

6. Conclusions

By employing a radial basis function neural network observer for online estimation and compensation of system nonlinearities and designing a sliding mode control law based on the observer's state measurements, the approach effectively resolves parameter uncertainties and unknown external disturbances in electro-hydraulic servo systems. This significantly enhances the system's position control accuracy and robustness. Furthermore, to suppress high-frequency noise and improve system stability and control performance, a low-pass filter is introduced to smooth the controller, enhancing its smoothness and stability. Simulation analysis thoroughly validates the effectiveness of the designed controller. Compared with PSOPID controllers and adaptive sliding mode variable structure controllers, the proposed controller demonstrates distinct advantages in performance metrics under various reference signals. It exhibits superior tracking performance and robustness, thereby proving its outstanding capability in nonlinear control of electro-hydraulic servo systems. However, this approach still has limitations: initial neural network weights rely on empirical data, failing to achieve fully adaptive optimization; real-time challenges arise from high-order system dimensionality scaling; and it inadequately addresses multi-source coupled disturbances and actuator failures. Future work will focus on optimizing network architecture and initialization through reinforcement learning or meta-learning, developing lightweight algorithms for low-cost hardware with real-time validation, and extending the approach to fault-tolerant and multi-actuator cooperative control. These efforts aim to further enhance system reliability and stability under complex operating conditions.

Use of AI tools declaration

The authors declare they have not used Artificial Intelligence (AI) tools in the creation of this article.

Acknowledgments

This research was supported by the major science and technology special project of Yunnan Science and Technology Department (202202AC080008).

Conflict of interest

The authors declare there is no conflict of interest.

References

1. Y. Fan, J. Shao, G. Sun, Optimized PID controller based on beetle antennae search algorithm for electro-hydraulic position servo control system, *Sensors*, **19** (2019), 2727. https://doi.org/10.3390/s19122727
2. J. Yao, Z. Jiao, D. Ma, L. Yan, High-accuracy tracking control of hydraulic rotary actuators with modeling uncertainties, *IEEE/ASME Trans. Mechatron.*, **19** (2013), 633–641. https://doi.org/10.1109/TMECH.2013.2252360
3. F. Cao, PID controller optimized by genetic algorithm for direct-drive servo system, *Neural Comput. Appl.*, **32** (2020), 23–30. https://doi.org/10.1007/s00521-018-3739-z

4. D. Tavernini, F. Vacca, M. Metzler, D. Savitski, V. Ivanov, P. Gruber, et al., An explicit nonlinear model predictive ABS controller for electro-hydraulic braking systems, *IEEE Trans. Ind. Electron.*, **67** (2019), 3990–4001. https://doi.org/10.1109/TIE.2019.2916387
5. H. Feng, W. Ma, C. Yin, D. Cao, Trajectory control of electro-hydraulic position servo system using improved PSO-PID controller, *Autom. Constr.*, **127** (2021), 103722. https://doi.org/10.1016/j.autcon.2021.103722
6. J. Yao, Model-based nonlinear control of hydraulic servo systems: Challenges, developments and perspectives, *Front. Mech. Eng.*, **13** (2018), 179–210. https://doi.org/10.1007/s11465-018-0464-3
7. B. Yao, F. Bu, J. Reedy, G. Chin, Adaptive robust motion control of single-rod hydraulic actuators: theory and experiments, *IEEE/ASME Trans. Mechatron.*, **5** (2000), 79–91. https://doi.org/10.1109/3516.828592
8. K. Ba, B. Yu, Z. Gao, Q. Zhu, G. Ma, X. Kong, An Improved Force-based Impedance Control Method for the HDU of Legged Robots, *ISA Trans.*, **84** (2019), 187–205. https://doi.org/10.1016/j.isatra.2018.09.002
9. G. Wrat, M. Bhola, P. Ranjan, S. K. Mishra, J. Das, Energy saving and Fuzzy-PID position control of electro-hydraulic system by leakage compensation through proportional flow control valve, *ISA Trans.*, **101** (2020), 269–280. https://doi.org/10.1016/j.isatra.2020.01.003
10. G. Yang, J. Yao, Nonlinear adaptive output feedback robust control of hydraulic actuators with largely unknown modeling uncertainties, *Appl. Math. Modell.*, **79** (2020), 824–842. https://doi.org/10.1016/j.apm.2019.10.062
11. C. Luo, J. Yao, J. Gu, Extended-state-observer-based output feedback adaptive control of hydraulic system with continuous friction compensation, *J. Franklin Inst.*, **356** (2019), 8414–8437. https://doi.org/10.1016/j.jfranklin.2019.08.015
12. M. Khodaverdian, M. Malekzadeh, Fault-tolerant model predictive sliding mode control with fixed-time attitude stabilization and vibration suppression of flexible spacecraft, *Aerosp. Sci. Technol.*, **139** (2023), 108381. https://doi.org/10.1016/j.ast.2023.108381
13. K. Walid, M. Sofiane, H. Benbouhenni, G. Hamza, T. Es-saadi, Application of third-order sliding mode controller to improve the maximum power point for the photovoltaic system, *Energy Rep.*, **9** (2023), 5372–5383. https://doi.org/10.1016/j.egyr.2023.04.366
14. X. Shen, J. Liu, Z. Liu, Y. Gao, J. I. Leon, S. Vazquez, Sliding-mode control of neutral-point-clamped power converters with gain adaptation, *IEEE Trans. Power Electron.*, **39** (2024), 9189–9201. https://doi.org/10.1109/TPEL.2024.3386800
15. H. Liang, J. Zou, K. Zuo, M. J. Khan, An improved genetic algorithm optimization fuzzy controller applied to the wellhead back pressure control system, *Mech. Syst. Signal Process.*, **142** (2020), 106708. https://doi.org/10.1016/j.ymssp.2020.106708
16. H. Zhang, L. Wang, W. Shi. Seismic control of adaptive variable stiffness intelligent structures using fuzzy control strategy combined with LSTM, *J. Build. Eng.*, **78** (2023), 107549. https://doi.org/10.1016/j.jobe.2023.107549
17. H. Benbouhenni, N. Bizon, M. I. Mosaad, I. Colak, A. B. Djilali, H. Gasmi, Enhancement of the power quality of DFIG-based dual-rotor wind turbine systems using fractional order fuzzy controller, *Expert Syst. Appl.*, **238** (2024), 121695. https://doi.org/10.1016/j.eswa.2023.121695
18. G. Wen, C. L. P. Chen, S. S. Ge, Simplified optimized backstepping control for a class of nonlinear strict-feedback systems with unknown dynamic functions, *IEEE Trans. Cybern.*, **51** (2020), 4567–4580. https://doi.org/10.1109/TCYB.2020.3002108

19. K. Zheng, Q. Zhang, Y. Hu, B. Wu, Design of fuzzy system-fuzzy neural network-backstepping control for complex robot system, *Inf. Sci.*, **546** (2021), 1230–1255. https://doi.org/10.1016/j.ins.2020.08.110
20. H. Liu, Y. Pan, J. Cao, H. Wang, Y. Zhou, Adaptive neural network backstepping control of fractional-order nonlinear systems with actuator faults, *IEEE Trans. Neural Networks Learn. Syst.*, **31** (2020), 5166–5177. https://doi.org/10.1109/TNNLS.2020.2964044
21. L. Liao, B. Li, Y. Wang, Y. Xi, D. Zhang, L. Gao, Adaptive fuzzy robust control of a bionic mechanical leg with a high gain observer, *IEEE Access*, **9** (2021), 134037–134051. https://doi.org/10.1109/ACCESS.2021.3091132
22. Z. Wang, L. Yang, H. Ouyang, L. Yu, Global robust control of overhead cranes with distributed mass beams considering model uncertainty and external disturbance, *Mech. Syst. Signal Process.*, **214** (2024), 111378. https://doi.org/10.1016/j.ymssp.2024.111378
23. R. Yu, Y. Zhao, G. Wang, Y. H. Chen, C. Li, An intelligent cooperative game approach for adaptive robust control of fuzzy mechanical systems, *IEEE Trans. Fuzzy Syst.*, **32** (2024), 3594–3607. https://doi.org/10.1109/TFUZZ.2024.3376694
24. J. Tang, J. Cao, M. Wu, L. Zhao, F. Zhang, Position control of electro-hydraulic servo system using active disturbance rejection control for upper-limb exoskeleton, *J. Vibroeng.*, **25** (2023), 581–593. https://doi.org/10.21595/jve.2022.22850
25. Q. Zhu, D. Huang, B. Yu, K. Ba, X. Kong, S. Wang, An improved method combined SMC and MLESO for impedance control of legged robots' electro-hydraulic servo system, *ISA Trans.*, **130** (2022), 598–609. https://doi.org/10.1016/j.isatra.2022.03.009
26. Q. Zhu, J. Zhang, X. Li, H. Zong, B. Yu, K. Ba, et al., An adaptive composite control for a hydraulic actuator impedance system of legged robots, *Mechatronics*, **91** (2023), 102951. https://doi.org/10.1016/j.mechatronics.2023.102951
27. Y. Wang, X. Wang, B. Fu, J. Ruan, S. An, Kinematics analysis of a FLHL robot parallel-executed cylinder mechanical integration system with force/position hybrid control servo actuator, *J. Vibroeng.*, **23** (2021), 687–707. https://doi.org/10.21595/jve.2021.21833
28. T. Qin, Y. Li, L. Quan, L. Yang, An adaptive robust impedance control considering energy-saving of hydraulic excavator boom and stick systems, *IEEE/ASME Trans. Mechatron.*, **27** (2022), 1928–1936. https://doi.org/10.1109/TMECH.2022.3173991
29. C. Wang, J. Wang, Q. Guo, Z. Liu, C. L. P. Chen, Disturbance observer-based fixed-time event-triggered control for networked electro-hydraulic systems with input saturation, *IEEE Trans. Ind. Electron.*, **72** (2025), 1784–1794. https://doi.org/10.1109/TIE.2024.3429638
30. H. Feng, Q. Song, S. Ma, W. Ma, C. Yin, D. Cao, et al., A new adaptive sliding mode controller based on the RBF neural network for an electro-hydraulic servo system, *ISA Trans.*, **129** (2022), 472–484. https://doi.org/10.1016/j.isatra.2021.12.044
31. Q. Guo, H. Zhan, Z. Wang, T Li, Fixed-time sliding mode adaptive control of hydraulic manipulator with shutoff deadzone and uncertain nonlinearity, *IEEE Trans. Syst. Man Cybern.: Syst.*, **55** (2025), 7566–7578. https://doi.org/10.1109/TSMC.2025.3598080
32. V. Kumar, K. P. S. Rana. A novel fuzzy PID controller for nonlinear active suspension system with an electro-hydraulic actuator, *J. Braz. Soc. Mech. Sci. Eng.*, **45** (2023), 189. https://doi.org/10.1007/s40430-023-04095-z

33. M. F. Ghani, R. Ghazali, H. I. Jaafar, C. C. Soon, Y. M. Sam, Z. Has, Fractional order integral sliding mode tracking control of a third-order double-acting electrohydraulic actuator model, *Int. J. Mech. Eng. Rob. Res.*, **11** (2022), 669–675. https://doi.org/10.18178/ijmerr.11.9.669-675
34. A. A. Khater, M. Fekry, M. El-Bardini, A. M. EI-Nagar, Deep reinforcement learning-based adaptive fuzzy control for electro-hydraulic servo system, *Neural Comput. Appl.*, **37** (2025), 1–18. https://doi.org/10.1007/s00521-024-10741-x
35. S. Ahmadi, S. Abdi, M. Kakavand, Maximum power point tracking of a proton exchange membrane fuel cell system using PSO-PID controller, *Int. J. Hydrogen Energy*, **42** (2017), 20430–20443. https://doi.org/10.1016/j.ijhydene.2017.06.208
36. Y. Huang, T. Kuo, S. Chang, Adaptive sliding-mode control for nonlinearsystems with uncertain parameters, *IEEE Trans. Syst. Man Cybern. Part B Cybern.*, **38** (2008), 534–539. https://doi.org/10.1109/TSMCB.2007.910740

AIMS Press

©2025 the Author(s), licensee AIMS Press. This is an open access article distributed under the terms of the Creative Commons Attribution License (https://creativecommons.org/licenses/by/4.0)